

Article

# Growth of WS<sub>2</sub> flakes on Ti<sub>3</sub>C<sub>2</sub>T<sub>x</sub> Mxene Using Vapor Transportation Routine

Weitao Su <sup>1,\*</sup>, Shengguang Wang <sup>1</sup>, Li Fu <sup>1</sup>, Fei Chen <sup>1</sup>, Kaixin Song <sup>2</sup>, Xiwei Huang <sup>2</sup>   
and Li Yang <sup>3</sup>

<sup>1</sup> College of Materials and Environmental Engineering, Hangzhou Dianzi University, Hangzhou 310018, China; wsg392339396@163.com (S.W.); fuli@hdu.edu.cn (L.F.); chenfei@hdu.edu.cn (F.C.)

<sup>2</sup> College of Electronics and Information, Hangzhou Dianzi University, Hangzhou 310018, China; kxsong@hdu.edu.cn (K.S.); huangxiwei@hdu.edu.cn (X.H.)

<sup>3</sup> Department of Chemistry, Xi'an Jiaotong-Liverpool University, Suzhou 215123, China; Li.Yang@xjtlu.edu.cn

\* Correspondence: suweitao@hdu.edu.cn

Received: 1 July 2018; Accepted: 11 August 2018; Published: 14 August 2018



**Abstract:** Two-dimensional dichalcogenides (TMDs) and mxene junctions had been predicted to possess distinct tunable electronic properties. However, direct synthesis of WS<sub>2</sub> on Ti<sub>3</sub>C<sub>2</sub>T<sub>x</sub> mxene is still challenging. Herein, we successfully deposited WS<sub>2</sub> onto the surface of Ti<sub>3</sub>C<sub>2</sub>T<sub>x</sub> mxene by employing the vapor transportation (VT) routine. By modulating pressure and source-sample distance, multilayer and monolayer (1 L) WS<sub>2</sub> flakes were deposited onto the lateral side and top surface of Ti<sub>3</sub>C<sub>2</sub>T<sub>x</sub> flakes. The 1 L WS<sub>2</sub> flakes growing on lateral side of Ti<sub>3</sub>C<sub>2</sub>T<sub>x</sub> flake have much higher photoluminescence (PL) intensity than 1 L flakes growing on the top surface. Our study has the potential to benefit the design and preparation of novel electronic and electrochemical devices based on TMDs/mxene junctions.

**Keywords:** vapor transportation; 1 L WS<sub>2</sub>; Ti<sub>3</sub>C<sub>2</sub>T<sub>x</sub> mxene

## 1. Introduction

As an important member of TMDs, WS<sub>2</sub> has recently received much attention owing to its distinguished electronic and optical properties [1–3]. WS<sub>2</sub> possesses a periodic layer structure, in which each layer is composed by a plane of tungsten atoms sandwiched between two planes of sulphur atoms [3]. Bulk WS<sub>2</sub> and several layer WS<sub>2</sub> flakes have indirect band structures with a band gap of ~1.4 eV [3]. When the flake thickness of WS<sub>2</sub> is reduced to 1 L (~0.7 nm) [3], its band structure transits into direct band with a much larger band gap (>2 eV) [3]. Large excitonic binding energy of WS<sub>2</sub> (320 meV) [1] enables the observation of excitonic PL with peak position of ~2 eV, even at room temperature. 1 L WS<sub>2</sub> exhibits high PL (photoluminescence) quantum yield (~3%) [2], which is an order of magnitude higher than that of 1 L MoS<sub>2</sub> [4]. Such properties indicate that 1 L WS<sub>2</sub> is a potential candidate in novel high quantum yield (QY) light emitting diodes (LEDs) [5] and ultrathin light sources [6].

In contrast to TMDs, Ti<sub>3</sub>C<sub>2</sub> mxene has recently also drawn much attention owing to its high conductivity as  $4.2 \times 10^{-4}$  S/m [7–9]. The Ti<sub>3</sub>C<sub>2</sub> mxene is also a layered structure material within which each layer contains two carbon atom planes sandwiched between three Ti atom planes [10]. Differing from WS<sub>2</sub>, the conduction band minima of Ti<sub>3</sub>C<sub>2</sub> mxene touches the valance band maxima at  $\Gamma$  point, indicating Ti<sub>3</sub>C<sub>2</sub> mxene is a half-metallic material [10]. The attachment of surface functional groups (annotated as “T”) [10], such as –F, –O and –OH, etc. [11], generated in solution etching of M<sub>n</sub>AlC<sub>n+1</sub> phase [11] also slightly opens up the band gap of Ti<sub>3</sub>C<sub>2</sub>T<sub>x</sub> mxene [10].

A heterostructure composed by mxene and TMDs had been predicted to have tunable band structures [12,13]. Ma et al. [13] predicted the band gap of  $\text{Sc}_2\text{CF}_2/\text{TMDs}$  can be largely tuned from 0.13 to 1.18 eV by using density function theory (DFT) calculations. Li et al. calculated the band structure of  $\text{MoS}_2/\text{M}_2\text{CO}_2$  ( $\text{M} = \text{Ti}, \text{Sc}$  and  $\text{Hf}$ ) and also found these heterostructures show a large tunable band gap as 0.25–1.67 eV [12]. Moreover,  $\text{MoS}_2/\text{Zr}_2\text{CO}_2$  was predicted to exhibit an interesting type-II semiconductor feature with conduction and valance bands in different layers [12]. These distinct properties intrigued their applications in novel devices. Wu et al. used  $\text{MoS}_2$  decorated  $\text{Ti}_3\text{C}_2$  mxene as electrode and greatly enhanced the capacity of sodium-ion batteries [14]. Xu et al. used  $\text{Ti}_2\text{C}(\text{OH})_x\text{F}_y$  as a novel electrode material and greatly reduced the Schottky barrier height between electrode and  $\text{WSe}_2$  [15]. Regarding this progress, the  $\text{WS}_2/\text{Ti}_3\text{C}_2\text{T}_x$  structure had not been synthesized. The basic material properties of this novel structure are still unknown. In this study, we deposited  $\text{WS}_2$  flakes on  $\text{Ti}_3\text{C}_2\text{T}_x$  mxene using a VT (vapor transportation) routine. The thickness of  $\text{WS}_2$  layer on  $\text{Ti}_3\text{C}_2\text{T}_x$  mxene can be tuned by changing the pressure inside the tube. Our experimental results could be indicative to the preparation of novel TMDs/Mxene heterostructures, and would benefit the preparation of devices based on this novel structure.

## 2. Materials and Methods

### 2.1. Sample Preparation

The VT routine was employed to deposit  $\text{WS}_2$  flakes. A schematic of deposition is shown in Figure 1a. For direct deposition of  $\text{WS}_2$  on  $\text{Si}/\text{SiO}_2$  (300 nm) substrates, the substrates were cleaned by deionized water, ethanol, and  $\text{H}_2\text{O}_2$ . For deposition of  $\text{WS}_2$  on mxene,  $\text{Ti}_3\text{C}_2\text{T}_x$  mxene prepared by standard procedure [16] (with a yield of ~72%) was ultrasonically exfoliated (700 W of ultrasonic power) for 1 h and spin coated on cleaned  $\text{Si}/\text{SiO}_2$  (300 nm) substrates. The typical size of ultrasonically exfoliated  $\text{Ti}_3\text{C}_2\text{T}_x$  mxene flakes on the substrate was 3–5  $\mu\text{m}$ . The  $\text{WS}_2$  powders and substrates were loaded in a one-zone tube furnace with quartz tube diameter of 1 inch. The  $\text{WS}_2$  source was put at the center of the heating zone. The substrate was put at the down-steam low temperature area and the source-substrate distance was kept as 12 cm by moving the substrate. The source temperature was raised from room temperature to 1000 °C within 50 min, then held for 60 min, and finally cooled to ambient temperature naturally. Pure nitrogen gas with flow rate of 20 sccm was used as carrier gas.

### 2.2. Characterization

The optical images of  $\text{WS}_2$  and  $\text{Ti}_3\text{C}_2\text{T}_x$  mxene were obtained using an optical microscope. Micro Raman and PL measurements were conducted on a home built Raman/PL system, consisting of an inverted microscope (Ti eclipse, Nikon, Tokyo, Japan) and a Raman spectrometer (iHR320, Horiba, Palaiseau, France) attached with a CCD detector (Syncerity, Horiba, Palaiseau, France). A 532 nm laser was focused onto the sample using a 100 $\times$ , 0.95 NA objective lens. The PL intensity images were recorded by a photoluminescence microscope with excitations of LED (light-emitting diode, central wavelength of 485 nm). The topographic images of samples were measured by an atomic force microscope (Innova, Bruker, Karlsruhe, Germany). Scanning electron microscopy (SEM) images were collected on a Hitachi JSM-6460 SEM (Hitachi, Tokyo, Japan).

$\text{Ti}_3\text{C}_2\text{T}_x$  mxene has birefringence property [17]. The polarization direction of light reflected from mxene is altered to an angle differing to that of the incident light. However, this cannot occur with dust or  $\text{WS}_2$ . Such an effect allows for the identification of  $\text{Ti}_3\text{C}_2\text{T}_x$  flakes from other objects (i.e., dusts) by using polarization optical microscope. At parallel configuration, i.e., where the polarization directions of two polarizers at incident and out-going light path of the microscope are parallel to each other, both  $\text{Ti}_3\text{C}_2\text{T}_x$  flakes and other objects without birefringence property can be seen (Figure S1a). However, at cross configuration, i.e., where the polarization directions of two polarizers are perpendicular to each other, the reflected light from objects without birefringence is blocked, while only  $\text{Ti}_3\text{C}_2\text{T}_x$  flakes are visible (Figure S1b). This simple method can also be used to distinguish  $\text{WS}_2$  flakes growing on

$\text{Ti}_3\text{C}_2\text{T}_x$  from those grown on  $\text{SiO}_2$  and dusts. The 1 L  $\text{WS}_2$  flakes growing around  $\text{Ti}_3\text{C}_2\text{T}_x$  flakes show light purple contrast at parallel configuration (Figure S1c), while becoming invisible at cross configuration (Figure S1d). However, the  $\text{Ti}_3\text{C}_2\text{T}_x$  flakes still show features similar to Figure S1b, i.e., bright contrast in cross configuration (Figure S1d).

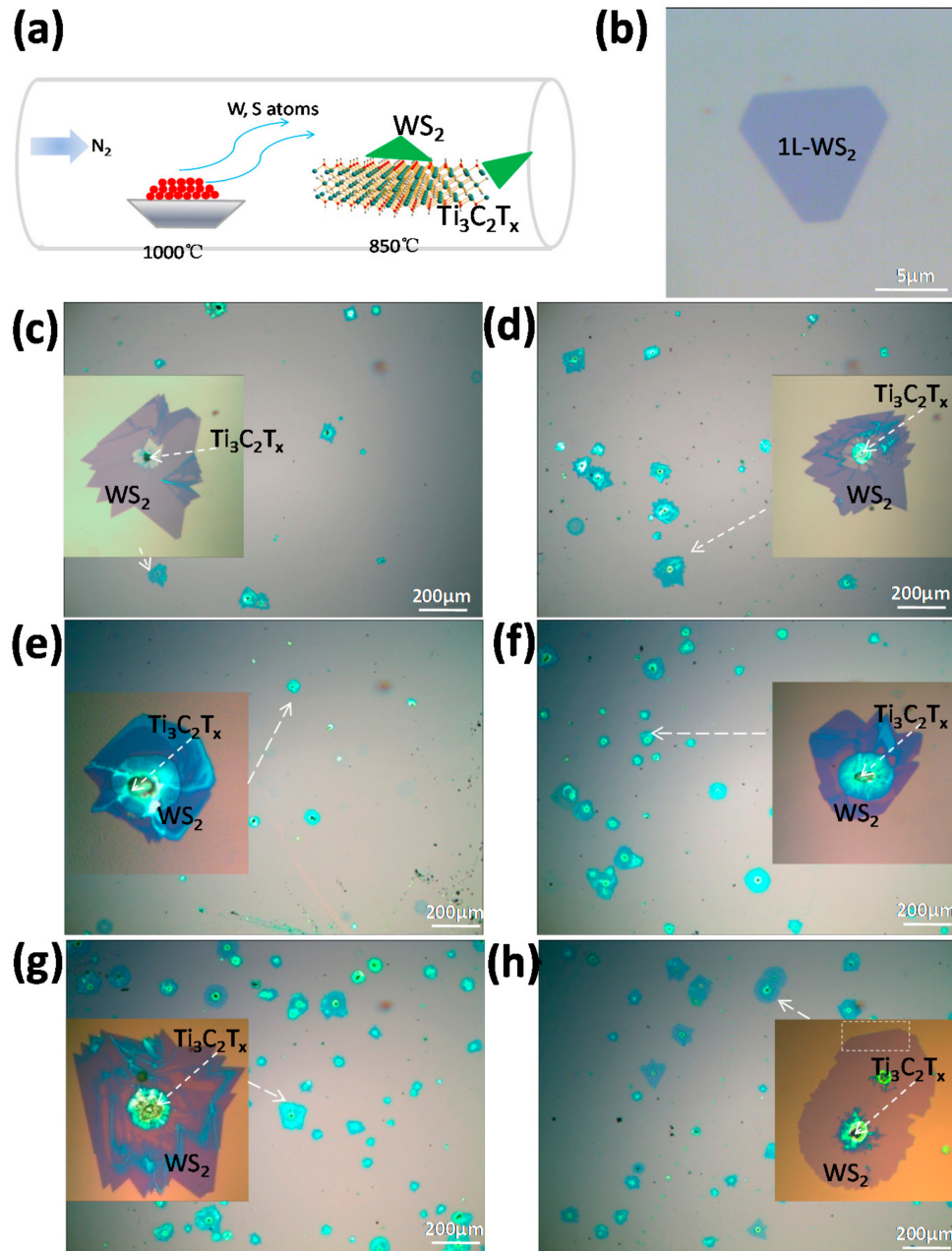


**Figure 1.** (a) Schematic of vapor transportation setup used in this study; (b) optical image of a  $\text{WS}_2$  1 L flake deposited without  $\text{Ti}_3\text{C}_2\text{T}_x$  mxene; Optical image of  $\text{WS}_2$  flakes deposited at (c) 200 Torr and (d) 250 Torr. Optical images of  $\text{WS}_2$  growing at 350 Torr and different substrate-source distance (e) 10 cm, (f) 10.5 cm, (g) 11 cm and (h) 11.5 cm. The insets give magnified images of the marked flakes.

### 3. Results and Discussion

#### 3.1. Growth of $WS_2/Ti_3C_2T_x$ Mxene

An optical image of a truncated triangular  $WS_2$  flake deposited without  $Ti_3C_2T_x$  is shown in Figure 1b. Light purple contrast indicates that this is a 1 L flake, which can be confirmed by its single excitonic band with strong PL intensity (shown in the following sections). The growth of  $WS_2$  on  $Ti_3C_2T_x$  mxene strongly depends on the deposition pressure and the sample-source distance ( $D$ ). The optical images of  $WS_2$  deposited with  $Ti_3C_2T_x$  mxene at pressures of 200 Torr and 250 Torr are shown in Figure 1c,d, respectively. At a low pressure of 200 Torr, the size of flake growing around mxene is quite small. Larger flakes with 1 L and few layers can be observed at high pressures as 250 Torr (Figure 1d) and 350 Torr (Figure 1e–h). The growth of  $WS_2$  flake also strongly depends on  $D$ . Figure 1e–h shows images of flakes with  $D$  of 9 cm, 9.5 cm, 10 cm, and 10.5 cm, respectively. At short  $D$  (9 cm) (Figure 1e), the  $WS_2$  tends to grow into thick flakes, while at long  $D$  (10.5–11 cm), 1 L  $WS_2$  flakes can be obtained (Figure 1g,h). It should be noted that at even larger  $D$  ( $D > 11$  cm),  $WS_2$  islands instead of flakes are observed. An AFM topographic image of a 1 L  $WS_2$  flake area marked in Figure 1h is shown in Figure S2a. This 1 L  $WS_2$  flake is quite flat within the flake area. High density of nanocrystals can be observed at the  $WS_2$  flake edge and on the blank  $SiO_2$ . These nanocrystals, which are usually found during vapor transportation growth [18], can be assigned to  $WS_2$ . The thickness of 1 L  $WS_2$  can be determined to be  $\sim 0.8$  nm from the line profile across the edge (Figure S2b), which agrees well with the reported thickness of a 1 L  $WS_2$  flake [19].

We also investigated the growth of  $WS_2$  flakes on the top of mxene flakes. Three typical SEM images are shown in Figure 2a–c. Figure 2a shows a situation in which  $WS_2$  grows on a flat  $Ti_3C_2T_x$  flake sitting on the substrate. In this case  $WS_2$  grows on the top surface of this  $Ti_3C_2T_x$  flake and finally uniformly covers the top surface. This indicates  $WS_2$  can nucleate and grow on the surface of  $Ti_3C_2T_x$  flake easily. Figure 2b corresponds to  $WS_2$  grows on a  $Ti_3C_2T_x$  flake with terrace-like edges. In this image, the  $WS_2$  layer covers both the top surface and the lateral side of terrace-like edges. The disappearance of  $Ti_3C_2T_x$  edges in Figure 2a,b indicates the  $WS_2$  covers the whole lateral side. Figure 2c shows a feature slightly differing from Figure 2b: despite the  $WS_2$  coated on the lateral side of this  $Ti_3C_2T_x$  flake, many small petals also grow on the top and the lateral side. Based on Figure 2a–c, a possible growth model is proposed, and is schematically shown in Figure 2d. In this simple model, a bilayer  $Ti_3C_2T_x$  flake lies on the substrate. The  $Ti_3C_2T_x$  flake acts as an inhomogeneous nucleation agent, similar to the other precursors such as graphene and BN used in the growth of 1 L  $MoS_2$  and  $WS_2$  [20–22]. In inhomogeneous nucleation procedure,  $WS_2$  nucleates much more easily than the homogeneous nucleation owing to the reduced free energy [23]. The seeds of  $WS_2$  on the top surface and lateral side grow, and finally merge into a  $WS_2$  layer covering the whole surface of  $Ti_3C_2T_x$  mxene. The thickness of the top layer, which can be determined from their Raman and PL spectra (see following section for further discussions), also greatly depends on the growth conditions. Similar to other precursors again, the  $Ti_3C_2T_x$  flake is also a good inhomogeneous nucleation agent for growth of  $WS_2$  flakes on  $SiO_2/Si$  substrate. Triangular flakes nucleating on some sites eat up the small islands surrounding the flake by diffusion and finally grow into a big  $WS_2$  flake. The final shape of this flake greatly depends on the number of nucleation sites. For few nucleation sites (such as Figure 1h), simple triangular flakes can be obtained, while for a  $Ti_3C_2T_x$  flake with large number of nucleation sites, a polygon shape flake with a number of corners can be obtained (Figure 1g).

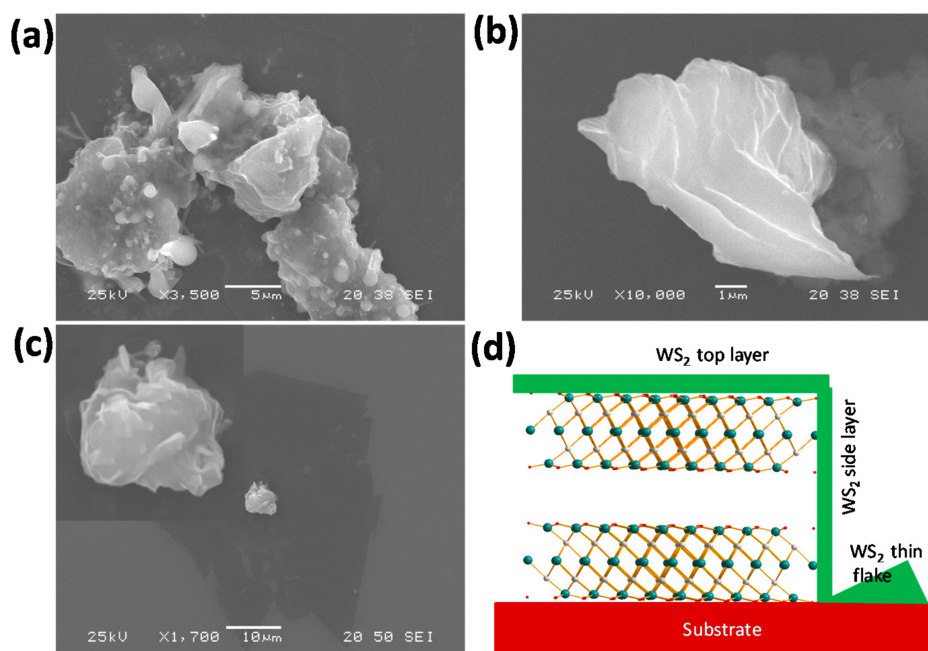


**Figure 2.** Morphology of WS<sub>2</sub> flakes growing on different Ti<sub>3</sub>C<sub>2</sub>T<sub>x</sub> flakes (a–c); (d) Schematic of possible growth mechanism of WS<sub>2</sub> on Ti<sub>3</sub>C<sub>2</sub>T<sub>x</sub> flakes. The inset of Figure 2c shows the magnified SEM image of WS<sub>2</sub> petals on Ti<sub>3</sub>C<sub>2</sub>T<sub>x</sub>. Note the flakes in (a–c) are chosen from samples deposited at 350 Torr.

### 3.2. Optical Characterization of WS<sub>2</sub>/Ti<sub>3</sub>C<sub>2</sub>T<sub>x</sub> Mxene

In order to investigate the optical properties of WS<sub>2</sub> growing on Ti<sub>3</sub>C<sub>2</sub>T<sub>x</sub> mxene, five WS<sub>2</sub> flakes named by T1–T5 are selected from Figure 1e–h, and their optical images are shown in Figure 3a–e, respectively. From T1 to T5, the optical contrast changes from high contrast (T1, Figure 3a) to deep purple (T2 in Figure 3b and T3 in Figure 3c), and finally light purple (T4 in Figure 3d and T5 in Figure 3e), which indicates T1 is a thick-layer (TL) flake, T2 and T3 are few layer (FL) flakes, while T4 and T5 are 1 L flakes. Raman spectra collected from locations LT1–LT5 marked on flakes T1–T5 are shown in Figure 3f. A Raman spectrum of 1 L WS<sub>2</sub> in Figure 1b is also shown for comparison. At a laser excitation wavelength of 532 nm, the Raman spectra of WS<sub>2</sub> flakes exhibit features of first-order and second-order blended Raman modes, which are similar to previous reports [19,24]. The Raman peak at 417.8 cm<sup>-1</sup> can be assigned to A<sub>1g</sub> (out-of-plane mode). The peak at 351.3 cm<sup>-1</sup> can be assigned to the blended modes of E<sub>2g</sub><sup>1</sup> (in-plane mode) and 2LA mode (M point of first Brillion zone). The Raman peaks at 324.1 and 296.2 cm<sup>-1</sup> can be assigned to second order Raman modes of 2LA – E<sub>2g</sub><sup>2</sup> and 2LA – 2E<sub>2g</sub><sup>2</sup>, respectively [19,24]. As the most distinguishable feature, the intensity of A<sub>1g</sub> peak subsequently decreases from LT1 to LT5. This agrees well with previous reports, and can be attributed to the decreasing layer thickness [25,26]. The shift of A<sub>1g</sub> peak can also be used to determine the layer thickness [25,26]. The A<sub>1g</sub> Raman peaks of flakes T1–T5 collected at LT1–LT5 are plotted in Figure S3a. A red shift of A<sub>1g</sub> peak can be observed with decreasing layer thickness. We further fitted the A<sub>1g</sub> peak by using a Lorentzian function. The obtained peak positions are shown in Figure S3b. For thick layer flake T1, the peak position of A<sub>1g</sub> is 419.2 cm<sup>-1</sup>, corresponding to the peak position of thick layer [25,26].

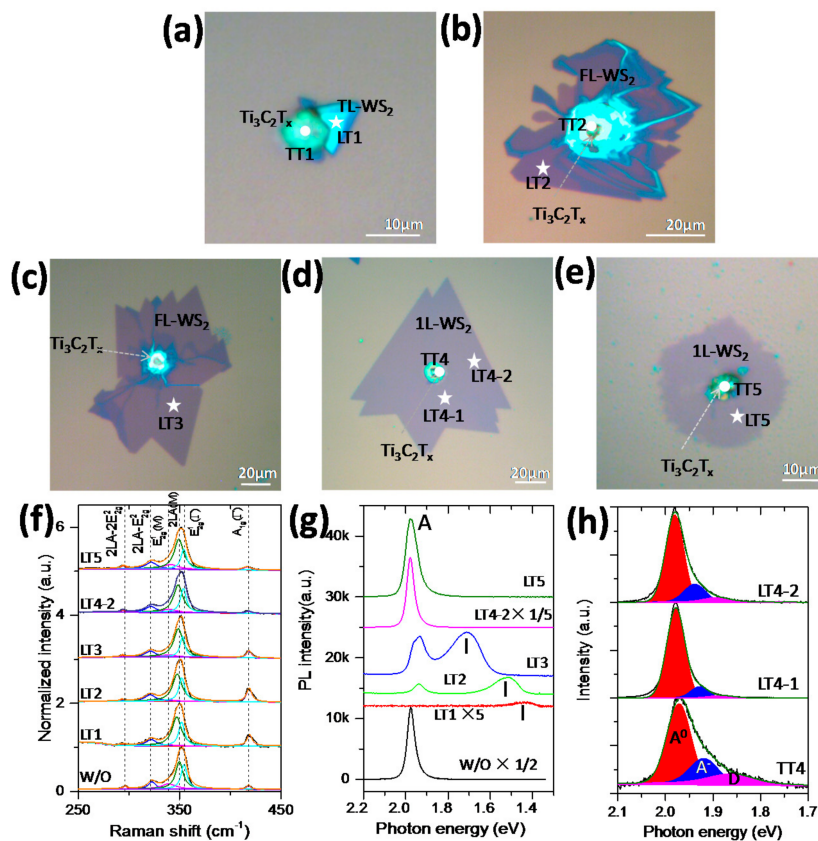


**Figure 3.** (a–e): optical images of five WS<sub>2</sub> flakes (T1–T5) with different thickness deposited with Ti<sub>3</sub>C<sub>2</sub>T<sub>x</sub> mxene; (f) Raman and (g) PL spectra of collected on locations LT1–LT5 on WS<sub>2</sub> flake T1–T5; (h) Deconvolution of PL spectra collected from different locations TT4, LT4-1 and LT4-2 (marked in (d)) of WS<sub>2</sub> flake T4. Note that the PL intensities of some flakes are divided by a factor for clear comparison. The Raman spectra are normalized for clear comparison. The Raman and PL spectra of 1 L-WS<sub>2</sub> deposited without mxene (W/O) in Figure 1b are also shown in (f,g), respectively, for comparison.

For flakes T2 and T3, the A<sub>1g</sub> peak shifts to 418.5 and 418 cm<sup>-1</sup>, indicating trilayer and bilayer of these two flakes [25,26], respectively. The average peak position of T4, T5, and 1 L flake deposition without mxene is 416.9 cm<sup>-1</sup>, confirming the 1 L characteristic of these three flakes [25,26].

PL spectra of WS<sub>2</sub> flakes growing surrounding the central Ti<sub>3</sub>C<sub>2</sub>T<sub>x</sub> flake of samples were also collected from locations LT1–LT5, and are shown in Figure 3g. For comparison, the PL spectrum of 1 L WS<sub>2</sub> flake in Figure 1b is also shown in Figure 3g. According to the previous reports [3,27], excitons generated by the direct band transition in 1 L WS<sub>2</sub> show a single PL peak, while double wavelet PL bands originating from excitonic transitions belonging to the direct band transition (K-K) and indirect band transition are always observed on few layer (layer numbers 2–4) WS<sub>2</sub> flakes. In the PL spectrum of 1 L flake in Figure 1b, the strong single PL peak centered at 1.98 eV can be assigned to A exciton band of 1 L WS<sub>2</sub>. Flake T1 shows a broad PL peak centered at 1.44 eV (marked as I), which fits the indirect excitonic transition energy of thick layer with layer numbers >4 layer [28]. The PL spectrum of T2 exhibits a broad peak at 1.52 eV and a sharp peak at 1.94 eV, which corresponds to the excitonic transition of indirect (I) and direct band (A), respectively [29]. The energy of indirect band transition agrees well with the indirect band transition energy of trilayer WS<sub>2</sub> flake [29]. Similar to T2, T3 shows two PL peaks at 1.94 eV and 1.72 eV, which correspond to the direct and the indirect excitonic transition bands, respectively, of bilayer very well [29]. Single excitonic peak feature of T4 and T5 at 1.98 eV agrees well with that of WS<sub>2</sub> deposited without mxene and the reported excitonic energy of 1 L WS<sub>2</sub>, confirming the 1 L nature of T4 and T5 [29,30]. It should be noted that the PL intensity of T5 is only

20% of T4. Meanwhile, its peak width of 68 meV is also larger than that of T4 (47 meV), which possibly be induced by high density of defects in T5 [31].

PL spectra are also measured on the top of  $\text{Ti}_3\text{C}_2\text{T}_x$  flakes coated with  $\text{WS}_2$  (locations TT1, TT2, TT4, and TT5 marked in Figure 3a,b,d,e), shown in Figure S4. Owing to the growth of  $\text{WS}_2$  on the top surface, these  $\text{Ti}_3\text{C}_2\text{T}_x$  flake exhibit PL characteristics of  $\text{WS}_2$  flakes. PL spectra collected from locations TT1 and TT2 show double PL bands, which indicates the  $\text{WS}_2$  growing on the top surfaces of mxenes in T1 and T2 are thick layers (Figure S4a). Single PL peaks with energies at 1.96 eV and 1.95 eV of locations TT4 and TT5 indicate the  $\text{WS}_2$  flakes growing on the top surface of mxenes in T4 and T5 are 1 L (Figure S4b). In Figure S4b, the  $\text{WS}_2$  flake on the top of a  $\text{Ti}_3\text{C}_2\text{T}_x$  flake shows a PL peak much broader (FWHM = 83 meV) than that of 1 L  $\text{WS}_2$  flake growing around this  $\text{Ti}_3\text{C}_2\text{T}_x$  flake (FWHM = 47 meV). The PL intensity of TT4 is greatly quenched by  $\sim 50$  times in contrast to that of LT4-1. On the PL spectra of TT4 and TT5, a long PL tail is observed at the low energy side. A further deconvolution of PL spectra collected at locations TT4 and LT4-1 of 1 L  $\text{WS}_2$  flake T4 was performed using three Gaussian functions, and is shown in Figure 3h. These three functions represent the neutral exciton ( $A^0$ ) at  $\sim 1.97$  eV, trion ( $A^-$ ) at  $\sim 1.92$  eV and exciton trapped on defects ( $D$ ) at  $\sim 1.86$  eV, respectively. In contrast to PL energy of LT4-1, the  $A^0$  exciton energy of TT4 redshifts by  $\sim 19$  meV. Meanwhile, the normalized PL intensity of  $A^-$  and  $D$  excitons of TT4 are also enhanced. Auger recombination at  $\text{WS}_2/\text{Ti}_3\text{C}_2\text{T}_x$  interface is the first possible reason quenching the PL intensity of TT4. The PL intensity of  $\text{MoS}_2$  can be greatly quenched at  $\text{MoS}_2/\text{graphene}$  [32] and  $\text{MoS}_2/\text{Au}$  [33] contact due to strong Auger recombination. The electric conductivity of  $\text{Ti}_3\text{C}_2\text{T}_x$  is  $4.2 \times 10^{-4}$  S/m [9], which is comparable to graphene. Similar to the PL quenching observed at graphene/TMD interface, the Auger recombination at  $\text{WS}_2/\text{Ti}_3\text{C}_2\text{T}_x$  interface can also greatly reduce the PL intensity of  $\text{WS}_2$  [32]. However, simple Ohmic contact of  $\text{WS}_2$  to conductor would not cause strongly enhanced  $D$  exciton signal [34,35]. Therefore, defects related nonradiative recombination should be considered as the second possible reason inducing PL quenching [36]. According to a study by Kim et al. [30], strong intensity of this PL tail indicates a high density of excitons trapped on defects. High intensity of  $D$  exciton peak indicates high density of defects of 1 L  $\text{WS}_2$  growing on mxene [37]. We suspect that this high density of defects reduces the PL intensity of  $A^0$  and  $A^-$  excitons via the non-recombination process [36]. In our previous study, we found the increasing density of Se adatoms can effectively reduce the band gap of 1 L  $\text{WSe}_2$  [38], inducing the redshift of excitonic energy. We suspect that observed red shift of  $A^0$  exciton of 1 L  $\text{WS}_2$  growing on  $\text{Ti}_3\text{C}_2\text{T}_x$  mxene is induced by the same factor. The dielectric constant of  $\text{Ti}_3\text{C}_2\text{T}_x$  ( $\epsilon_r = 2.5$  and  $\epsilon_i = 3.5$ ) [39] is slightly larger than that of  $\text{SiO}_2$  ( $\epsilon_r = 2.1$  and  $\epsilon_i = 0$ ) [40]. According to the study of Lin et al., increasing environmental dielectric constant causes blue shift of excitonic energy [41], which is contrary to red shift of the excitonic energy of  $\text{WS}_2$  deposited on  $\text{Ti}_3\text{C}_2\text{T}_x$  as comparison to that of  $\text{WS}_2$  deposited on  $\text{SiO}_2$ . Therefore, the dielectric screening effect can be ruled out.

A PL image of the 1 L  $\text{WS}_2$  flake in Figure 3d is shown in Figure 4a. Although the shape of this flake measured by PL imaging fits that measured by optical image (Figure 3d), the PL intensity varies greatly at different positions. The PL intensity is strong at the grain boundary and the interface between  $\text{WS}_2$  and  $\text{Ti}_3\text{C}_2\text{T}_x$ , but weak at other points. Normalized PL spectra of LT4-2 as comparison to LT4-1 are shown in Figure 3h. It can be seen the PL spectrum of LT4-1 is broader than LT4-2. Simultaneously, a blue shift of LT4-1 is observed in contrast to LT4-2. We further fit these two PL spectra using three Gaussian peaks, representing three exciton states of  $A^0$ ,  $A^-$  and  $D$  (shown in Figure 3h), respectively. It can be seen the  $D$  exciton band of LT4-1 is stronger than that of LT4-2. In previous reports of Kim et al. [30], Gutierrez et al. [3] and Peimyoo et al. [19], different authors observed PL enhancement at edges and grain boundaries of CVD (chemical vapor deposition) deposited 1 L  $\text{WS}_2$  flakes. They attributed this PL enhancement to the high density of sulphur vacancies at the edges and grain boundaries [3,19,30]. In our study, PL enhancement is observed inside 1 L flake, but absent at its edges (Figures 4a and S5). It should be mentioned that the 1 L flakes shown in Figures 4a and S5 are polycrystalline instead of single crystal. The areas with enhanced PL intensity are almost along the

grain boundary. We suspect this is caused by a different distribution of sulphur defects. The presence of  $\text{Ti}_3\text{C}_2\text{T}_x$  mxene induces high density of sulphur vacancies only at grain boundary, but not on the edges, which finally induces the high PL intensity at grain boundaries observed in Figure 4a. Moreover, the PL energy of LT4-1 slightly blue shifted by 3 meV compared to that of LT4-2. Such blueshift is similar to that on defect area of 1 L  $\text{WS}_2$  observed by Kim et al. [30]. This indicates that the defects on our sample are also similar to the sulphur vacancies existing on samples of Kim et al. [30].

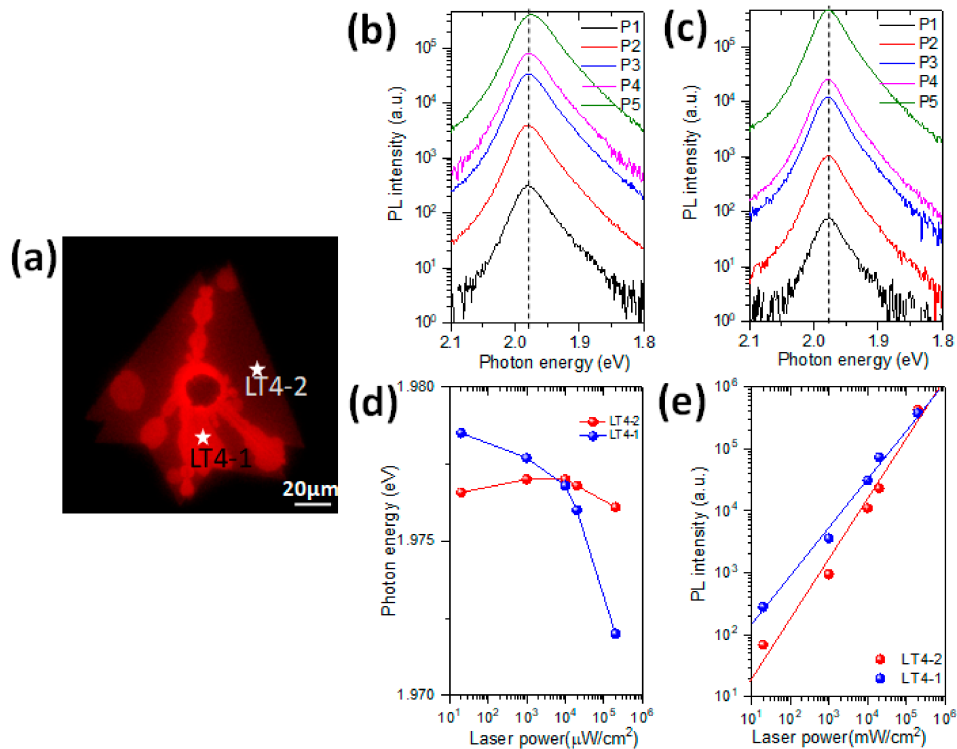


**Figure 4.** (a) Photoluminescence microscopy image of a  $\text{WS}_2$  1 L flake (flake T4 in Figure 3d), measured with LED irradiation, corresponding to low power); (b,c), PL spectra of points LT4-1 and LT4-2 with different laser power, respectively; (d) PL A band positions of points LT4-1 and LT4-2 at different excitation laser power density; (e) PL A band intensities of points LT4-1 and LT4-2 as a function of different laser power densities (symbols), fitting using a function of  $I = P^m$  (solid line). Note that in (b,c), the PL intensities are plotted in logarithmic scale to clearly show the PL intensity change. The laser powers are P1 = 0.02  $\mu\text{W}$ , P2 = 1  $\mu\text{W}$ , P3 = 10  $\mu\text{W}$ , P4 = 20  $\mu\text{W}$  and P5 = 200  $\mu\text{W}$ .

The laser power dependent PL of position LT4-1 and LT4-2 were measured at five different laser powers (0.02  $\mu\text{W}$ , 1  $\mu\text{W}$ , 10  $\mu\text{W}$ , 20  $\mu\text{W}$ , and 200  $\mu\text{W}$ ). Their obtained PL spectra are plotted in Figure 4b,c, respectively. At low excitation power (<20  $\mu\text{W}$ ), the PL intensity of LT4-1 is higher than that of LT4-2. At high excitation power, the measured PL intensity of LT4-2 becomes slightly stronger than LT4-1. The PL peak position as a function of excitation laser power density is plotted in Figure 4d. At low excitation power density, the PL energy of LT4-1 is higher than LT4-2. With increasing excitation laser power density, the peak energy of LT4-2 hardly shifts, while LT4-1 decreases faster. When the excitation laser power is higher than 10  $\mu\text{W}$ , the PL peak energy of LT4-1 becomes lower than LT4-2. This laser power dependent PL peak shift is very similar to that reported by Kim et al. [30]. In their study, the peak energy versus laser power curves of inner part of 1 L  $\text{WS}_2$  also intercepts with that of edge at  $\sim 10$   $\mu\text{W}$  [30]. It should be noted that the edges of  $\text{WS}_2$  samples used by Kim et al. have a higher density of defects than the inner parts [30]. Peak position versus laser power trend in our study is similar to that of Kim et al., indicating the role of defect at LT4-1 causing such PL energy shift.

As shown in Figure 3h, the intensities of  $A^-$  and  $D$  excitons are much lower than those of  $A^0$  exciton. Deconvolution of PL spectra measured at low laser power by using these three excitons always gives large uncertainty. Clear trends of PL intensity of different excitons versus excitation laser power are difficult to be obtained. However, the PL intensity of the whole  $A$  band versus laser power is straightforward and can be used for analysis. The PL intensity of  $A$  band measured at different laser power is clearly shown by a logarithmic plot (Figure 4f). We further fitted these data using the dependence  $I = P^m$ , where  $I$ ,  $P$  and  $m$  are PL intensity, laser power density, and numeric power [30,42]. The obtained  $m$  for LT4-1 and LT4-2 are 0.8 and 0.94, respectively. This sublinear dependence had been observed by different authors [30,43], indicating the role of defect. With a higher density of defects, more excitons generated at increasing laser power are trapped by defects, inducing low PL intensity increasing with laser power and a smaller  $m$  [43].

#### 4. Conclusions

In summary, we deposited  $WS_2$  thin flakes on  $Ti_3C_2T_x$  mxene using vapor transportation method.  $Ti_3C_2T_x$  mxene acts as good nucleation seed for  $WS_2$ .  $WS_2$  can easily nucleate and grow on the top surface and lateral edges of  $Ti_3C_2T_x$  mxene. By optimizing growth conditions, multilayer, few layer, and 1 L  $WS_2$  flakes can be deposited. A high density of defect is observed on 1 L  $WS_2$  flakes growing on the top surface of  $Ti_3C_2T_x$ , which greatly reduced their PL intensity. Our study would benefit the preparation of future 1 L  $WS_2/Ti_3C_2T_x$  junctions and their further potential applications in electronics devices.

**Supplementary Materials:** The following are available online at <http://www.mdpi.com/2079-6412/8/8/281/s1>, Figure S1: Optical image of a mxene flake at parallel (a) and cross (b) polarization; Optical image of a mxene coated with monolayer  $WS_2$  measured at parallel (c) and cross (d) polarization; Figure S2: (a) AFM image of a corner of a monolayer  $WS_2$  flake marked in Figure 1h; (b) the height profile of this flake along the dashed line in (a); Figure S3: (a)  $A1_g$  Raman peaks of different  $WS_2$  flakes; (b) The fitted  $A1_g$  peak positions of different  $WS_2$  flakes. W/O denotes the monolayer  $WS_2$  flake deposited without mxene; Figure S4: (a) PL spectra collected from locations TT1 and TT2 (marked in Figure 3a,b) the top of mxene in T1 and T2; (b) PL spectra collected from locations TT4 and TT5 (marked in Figure 3d,e) the top of mxene in T4 and T5; Figure S5: (a,c) Optical images of two monolayer  $WS_2$  flakes and their corresponding PL images (b,d), respectively.

**Author Contributions:** Conceptualization, W.S.; Methodology, W.S.; Writing—Original Draft Preparation, W.S.; Investigation, S.W., L.F., and F.C.; Formal analysis, K.S., L.Y., and X.H.

**Funding:** This research was funded by Zhejiang Provincial Natural Science Foundation of China (LY18F040006) and Natural Sciences Foundation of China (No. 61306115, 61775201, and 11404309).

**Acknowledgments:** The authors acknowledged Shichao Zhao (Hangzhou Dianzi University) for fruitful discussion of data processing.

**Conflicts of Interest:** The authors declare no conflict of interest.

#### References

1. Chernikov, A.; Berkelbach, T.C.; Hill, H.M.; Rigosi, A.; Li, Y.; Aslan, O.B.; Reichman, D.R.; Hybertsen, M.S.; Heinz, T.F. Exciton binding energy and nonhydrogenic rydberg series in monolayer  $WS_2$ . *Phys. Rev. Lett.* **2014**, *113*, 076802. [[CrossRef](#)] [[PubMed](#)]
2. Yuan, L.; Huang, L. Exciton dynamics and annihilation in  $WS_2$  2D semiconductors. *Nanoscale* **2015**, *7*, 7402–7408. [[CrossRef](#)] [[PubMed](#)]
3. Gutierrez, H.R.; Perea-Lopez, N.; Elias, A.L.; Berkdemir, A.; Wang, B.; Lv, R.; Lopez-Urias, F.; Crespi, V.H.; Terrones, H.; Terrones, M. Extraordinary room-temperature photoluminescence in triangular  $WS_2$  monolayers. *Nano Lett.* **2013**, *13*, 3447–3454. [[CrossRef](#)] [[PubMed](#)]
4. Mouri, S.; Miyauchi, Y.; Toh, M.; Zhao, W.; Eda, G.; Matsuda, K. Nonlinear photoluminescence in atomically thin layered  $WSe_2$  arising from diffusion-assisted exciton-exciton annihilation. *Phys. Rev. B* **2014**, *90*, 155499. [[CrossRef](#)]
5. Sundaram, R.S.; Engel, M.; Lombardo, A.; Krupke, R.; Ferrari, A.C.; Avouris, P.; Steiner, M. Electroluminescence in single layer  $MoS_2$ . *Nano Lett.* **2013**, *13*, 1416–1421. [[CrossRef](#)] [[PubMed](#)]

6. He, Y.M.; Clark, G.; Schaibley, J.R.; He, Y.; Chen, M.C.; Wei, Y.J.; Ding, X.; Zhang, Q.; Yao, W.; Xu, X.; et al. Single quantum emitters in monolayer semiconductors. *Nat. Nanotechnol.* **2015**, *10*, 497–502. [[CrossRef](#)] [[PubMed](#)]
7. Naguib, M.; Come, J.; Dyatkin, B.; Presser, V.; Taberna, P.L.; Simon, P.; Barsoum, M.W.; Gogotsi, Y. Mxene: A promising transition metal carbide anode for lithium-ion batteries. *Electrochem. Commun.* **2012**, *16*, 61–64. [[CrossRef](#)]
8. Come, J.; Naguib, M.; Rozier, P.; Barsoum, M.W.; Gogotsi, Y.; Taberna, P.L.; Morcrette, M.; Simon, P. A non-aqueous asymmetric cell with a  $Ti_2C$ -based two-dimensional negative electrode. *J. Electrochem. Soc.* **2012**, *159*, A1368–A1373. [[CrossRef](#)]
9. Han, M.; Yin, X.; Wu, H.; Hou, Z.; Song, C.; Li, X.; Zhang, L.; Cheng, L.  $Ti_3C_2$  mxenes with modified surface for high-performance electromagnetic absorption and shielding in the *x*-band. *ACS Appl. Mater. Interfaces* **2016**, *8*, 21011–21019. [[CrossRef](#)] [[PubMed](#)]
10. Tang, Q.; Zhou, Z.; Shen, P. Are mxenes promising anode materials for li ion batteries? Computational studies on electronic properties and Li storage capability of  $Ti_3C_2$  and  $Ti_3C_2X_2$  ( $X = F, OH$ ) monolayer. *J. Am. Chem. Soc.* **2012**, *134*, 16909–16916. [[CrossRef](#)] [[PubMed](#)]
11. Naguib, M.; Mashtalir, O.; Carle, J.; Presser, V.; Lu, J.; Hultman, L.; Gogotsi, Y.; Barsoum, M.W. Two-dimensional transition metal carbides. *ACS Nano* **2012**, *6*, 1322–1331. [[CrossRef](#)] [[PubMed](#)]
12. Li, X.; Dai, Y.; Ma, Y.; Liu, Q.; Huang, B. Intriguing electronic properties of two-dimensional  $MoS_2/TM_2CO_2$  ( $TM = Ti, Zr, \text{ or } Hf$ ) hetero-bilayers: Type-II semiconductors with tunable band gaps. *Nanotechnology* **2015**, *26*, 135703. [[CrossRef](#)] [[PubMed](#)]
13. Ma, Z.; Hu, Z.; Zhao, X.; Tang, Q.; Wu, D.; Zhou, Z.; Zhang, L. Tunable band structures of heterostructured bilayers with transition-metal dichalcogenide and mxene monolayer. *J. Phys. Chem. C* **2014**, *118*, 5593–5599. [[CrossRef](#)]
14. Wu, Y.; Nie, P.; Jiang, J.; Ding, B.; Dou, H.; Zhang, X.  $MoS_2$ -nanosheet-decorated 2D titanium carbide (mxene) as high-performance anodes for sodium-ion batteries. *Chemelectrochem* **2017**, *4*, 1560–1565. [[CrossRef](#)]
15. Xu, J.; Shim, J.; Park, J.H.; Lee, S. Mxene electrode for the integration of  $WSe_2$  and  $MoS_2$  field effect transistors. *Adv. Funct. Mater.* **2016**, *26*, 5328–5334. [[CrossRef](#)]
16. Naguib, M.; Kurtoglu, M.; Presser, V.; Lu, J.; Niu, J.; Heon, M.; Hultman, L.; Gogotsi, Y.; Barsoum, M.W. Two-dimensional nanocrystals produced by exfoliation of  $Ti_3AlC_2$ . *Adv. Mater.* **2011**, *23*, 4248–4253. [[CrossRef](#)] [[PubMed](#)]
17. Seyedin, S.; Yanza, E.R.S.; Razal, J.M. Knittable energy storing fiber with high volumetric performance made from predominantly mxene nanosheets. *J. Mater. Chem. A* **2017**, *5*, 24076–24082. [[CrossRef](#)]
18. Su, W.; Li, Y.; Jin, L.; Chen, L.; Song, K.; Huang, X.; Hong, X. Deposition of porous few-layer  $WSe_2$  flakes with high density of exposed edge sites. *Vacuum* **2017**, *145*, 4–10. [[CrossRef](#)]
19. Peimyoo, N.; Shang, J.; Cong, C.; Shen, X.; Wu, X.; Yeow, E.K.L.; Yu, T. Nonblinking, intense two-dimensional light emitter: Mono layer  $WS_2$  triangles. *ACS Nano* **2013**, *7*, 10985–10994. [[CrossRef](#)] [[PubMed](#)]
20. Okada, M.; Sawazaki, T.; Watanabe, K.; Taniguchi, T.; Hibino, H.; Shinohara, H.; Kitaura, R. Direct chemical vapor deposition growth of  $WS_2$  atomic layers on hexagonal boron nitride. *ACS Nano* **2014**, *8*, 8273–8277. [[CrossRef](#)] [[PubMed](#)]
21. Ling, X.; Lee, Y.H.; Lin, Y.; Fang, W.; Yu, L.; Dresselhaus, M.S.; Kong, J. Role of the seeding promoter in  $MoS_2$  growth by chemical vapor deposition. *Nano Lett.* **2014**, *14*, 464–472. [[CrossRef](#)] [[PubMed](#)]
22. Shi, Y.; Zhou, W.; Lu, A.Y.; Fang, W.; Lee, Y.H.; Hsu, A.L.; Kim, S.M.; Kim, K.K.; Yang, H.Y.; Li, L.J.; et al. Van der waals epitaxy of  $MoS_2$  layers using graphene as growth templates. *Nano Lett.* **2012**, *12*, 2784–2791. [[CrossRef](#)] [[PubMed](#)]
23. Zhang, D.; Wu, R. *Fundamentals of Materials Science*; Peking University Press: Beijing, China, 2011; Volume 1. (In Chinese)
24. He, Z.; Wang, X.; Xu, W.; Zhou, Y.; Sheng, Y.; Rong, Y.; Smith, J.M.; Warner, J.H. Revealing defect-state photoluminescence in monolayer  $WS_2$  by cryogenic laser processing. *ACS Nano* **2016**, *10*, 5847–5855. [[CrossRef](#)] [[PubMed](#)]
25. Berkdemir, A.; Gutierrez, H.R.; Botello-Mendez, A.R.; Perea-Lopez, N.; Elias, A.L.; Chia, C.I.; Wang, B.; Crespi, V.H.; Lopez-Urias, F.; Charlier, J.C.; et al. Identification of individual and few layers of  $WS_2$  using Raman spectroscopy. *Sci. Rep.* **2013**, *3*, 1755. [[CrossRef](#)]

26. Staiger, M.; Gillen, R.; Scheuschner, N.; Ochedowski, O.; Kampmann, F.; Schleberger, M.; Thomsen, C.; Maultzsch, J. Splitting of monolayer out-of-plane  $A_1'$  Raman mode in few-layer  $WS_2$ . *Phys. Rev. B* **2015**, *91*, 195419. [[CrossRef](#)]
27. Zhang, Y.; Zhang, Y.; Ji, Q.; Ju, J.; Yuan, H.; Shi, J.; Gao, T.; Ma, D.; Liu, M.; Chen, Y.; et al. Controlled growth of high-quality monolayer  $WS_2$  layers on sapphire and imaging its grain boundary. *ACS Nano* **2013**, *7*, 8963–8971. [[CrossRef](#)] [[PubMed](#)]
28. Zeng, H.; Liu, G.B.; Dai, J.; Yan, Y.; Zhu, B.; He, R.; Xie, L.; Xu, S.; Chen, X.; Yao, W.; et al. Optical signature of symmetry variations and spin-valley coupling in atomically thin tungsten dichalcogenides. *Sci. Rep.* **2013**, *3*, 1608. [[CrossRef](#)] [[PubMed](#)]
29. Zhao, W.; Ghorannevis, Z.; Chu, L.; Toh, M.; Kloc, C.; Tan, P.H.; Eda, G. Evolution of electronic structure in atomically thin sheets of  $WS_2$  and  $WSe_2$ . *ACS Nano* **2013**, *7*, 791–797. [[CrossRef](#)] [[PubMed](#)]
30. Kim, M.S.; Yun, S.J.; Lee, Y.; Seo, C.; Han, G.H.; Kim, K.K.; Lee, Y.H.; Kim, J. Biexciton emission from edges and grain boundaries of triangular  $WS_2$  monolayers. *ACS Nano* **2016**, *10*, 2399–2405. [[CrossRef](#)] [[PubMed](#)]
31. McCreary, A.; Berkdemir, A.; Wang, J.; Minh An, N.; Elias, A.L.; Perea-Lopez, N.; Fujisawa, K.; Kabiuss, B.; Carozo, V.; Cullen, D.A.; et al. Distinct photoluminescence and Raman spectroscopy signatures for identifying highly crystalline  $WS_2$  monolayers produced by different growth methods. *J. Mater. Res.* **2016**, *31*, 931–944. [[CrossRef](#)]
32. Shih, C.J.; Wang, Q.H.; Son, Y.; Jin, Z.; Blankschtein, D.; Strano, M.S. Tuning on-off current ratio and field-effect mobility in a  $MoS_2$ -graphene heterostructure via Schottky barrier modulation. *ACS Nano* **2014**, *8*, 5790–5798. [[CrossRef](#)] [[PubMed](#)]
33. Bhanu, U.; Islam, M.R.; Tetard, L.; Khondaker, S.I. Photoluminescence quenching in gold- $MoS_2$  hybrid nanoflakes. *Sci. Rep.* **2014**, *4*, 5575. [[CrossRef](#)] [[PubMed](#)]
34. Su, W.; Kumar, N.; Mignuzzi, S.; Crain, J.; Roy, D. Nanoscale mapping of excitonic processes in single-layer  $MoS_2$  using tip-enhanced photoluminescence microscopy. *Nanoscale* **2016**, *8*, 10564–10569. [[CrossRef](#)] [[PubMed](#)]
35. Kim, J.Y.; Kim, J.; Joo, J. Surface-enhanced Raman scattering for 2-D  $WSe_2$  hybridized with functionalized gold nanoparticles. *Opt. Express* **2016**, *24*, 27546–27553. [[CrossRef](#)] [[PubMed](#)]
36. Su, W.; Jin, L.; Qu, X.; Huo, D.; Yang, L. Defect passivation induced strong photoluminescence enhancement of rhombic monolayer  $MoS_2$ . *Phys. Chem. Chem. Phys.* **2016**, *18*, 14001–14006. [[CrossRef](#)] [[PubMed](#)]
37. Chow, P.K.; Jacobs-Gedrim, R.B.; Gao, J.; Lu, T.M.; Yu, B.; Terrones, H.; Koratkar, N. Defect-induced photoluminescence in mono layer semiconducting transition metal dichalcogenides. *ACS Nano* **2015**, *9*, 1520–1527. [[CrossRef](#)] [[PubMed](#)]
38. Su, W.; Li, Y.; Chen, L.; Huo, D.; Song, K.; Huang, X.; Shu, H. Nonstoichiometry induced broadband tunable photoluminescence of monolayer  $WSe_2$ . *Chem. Commun.* **2018**, *54*, 743–746. [[CrossRef](#)] [[PubMed](#)]
39. Berdiyrov, G.R. Optical properties of functionalized  $Ti_3C_2T_2$  (T = F, O, OH) mxene: First-principles calculations. *AIP Adv.* **2016**, *6*, 055105. [[CrossRef](#)]
40. Palik, E.D. *Handbook of Optical Constants of Solids*, 1st ed.; Academic Press: London, UK, 1998.
41. Lin, Y.; Ling, X.; Yu, L.; Huang, S.; Hsu, A.L.; Lee, Y.H.; Kong, J.; Dressehaus, M.S.; Palacios, T. Dielectric screening of excitons and trions in single-layer  $MoS_2$ . *Nano Lett.* **2014**, *14*, 5569–5576. [[CrossRef](#)] [[PubMed](#)]
42. Suh, J.; Tan, T.L.; Zhao, W.; Park, J.; Lin, D.Y.; Park, T.E.; Kim, J.; Jin, C.; Saigal, N.; Ghosh, S.; et al. Reconfiguring crystal and electronic structures of  $MoS_2$  by substitutional doping. *Nat. Commun.* **2018**, *9*, 199. [[CrossRef](#)] [[PubMed](#)]
43. Carozo, V.; Wang, Y.; Fujisawa, K.; Carvalho, B.R.; McCreary, A.; Feng, S.; Lin, Z.; Zhou, C.; Perea-Lopez, N.; Laura Elias, A.; et al. Optical identification of sulfur vacancies: Bound excitons at the edges of monolayer tungsten disulfide. *Sci. Adv.* **2017**, *3*, e1602813. [[CrossRef](#)] [[PubMed](#)]

